Cellulose (2021) 28:3359–3372
https://doi.org/10.1007/s10570-021-03740-x

ORIGINAL RESEARCH

# Mechanics of cellulose nanopaper using a scalable coarse-grained modeling scheme

**Upamanyu Ray · Zhenqian Pang · Teng Li**

Received: 14 October 2020 / Accepted: 28 January 2021 / Published online: 2 March 2021


**Abstract** Cellulose, the abundantly available and sustainable biopolymer, exhibits intrinsic mechanical properties superior to many high-performance structural materials. The exceptional mechanical properties of cellulose-based materials inherently hinge upon their bottom-up hierarchical material structure starting from cellulose molecular chains to large scale fibers. However, fully atomistic simulation of such materials at experimental sample dimension becomes computationally prohibitive for the exploration of mechanics involving length scale effects. To address this challenge, here we develop a bottom-up, scalable coarse-grained (CG) modeling scheme of cellulose materials to study the deformation and failure mechanism of cellulose-based materials with insight of the interplay among cellulose building blocks at different length scales, starting from molecular chain, to nanofiber, and finally to microfiber scales. After studying the response of cellulose fibers under different loadings such as shearing and opening, this CG scheme is applied to study the deformation process of a cellulose nanopaper under tension, thus revealing the nanoscale failure mechanism otherwise impossible by atomistic simulations. In addition, the CG model also predicts the strength and stiffness of the nanopaper with respect to varying fiber lengths. Given its scalable nature, such a CG modeling scheme can be readily adapted to study the mechanical behaviors of other cellulose-based materials with mechanistic insight from molecular scale, and thus holds promise to foster the design of cellulose-based high-performance materials.

**Keywords** Cellulose · Mechanics · Nanopaper · Coarse-grained modeling · Atomistic simulation · Molecular dynamics

## Introduction

Cellulose is gaining increasing attention due to a multitude of desirable properties such as high stiffness, strength and toughness, low density, and sustainability (Klemm et al. 2005; Ioelovich 2008; Kalia et al. 2011; Moon et al. 2011b; Dufresne 2017; Chen et al. 2020). Given the environmental issues related to high carbon footprint and emissions that exist in the 21st century, significant research efforts are invested in green, nature-inspired materials. The fact that cellulose is abundantly available from diverse natural sources such as plants, bacteria, tunicates and algae,

**Supplementary information** The online version contains supplementary material available at (https://doi.org/10.1007/s10570-021-03740-x)

U. Ray · Z. Pang (✉) · T. Li (✉)
Department of Mechanical Engineering, University of Maryland, College Park, MD 20742, USA
e-mail: zqpang@umd.edu

T. Li
e-mail: lit@umd.edu

makes it a desirable bio-based polymer for utilization in sustainable materials engineering. Currently, cellulose-based materials have been used in applications such as high-performance structural materials (Li et al. 2016; Zhu et al. 2016; Song et al. 2018b; Zhou et al. 2019), additive manufacturing (Sydney Gladman et al. 2016; Li et al. 2017), smart textiles (Jia et al. 2018), flexible and wearable electronics (Zhu et al. 2014a; Fang et al. 2019), energy storage (Zhang et al. 2017, 2019; Song et al. 2018a), thermal management (Diaz et al. 2014), microfluidics (Shin and Hyun 2017), biomedical devices (Czaja et al. 2007), tissue engineering (Svensson et al. 2005; Müller et al. 2006) and thermal management (Li et al. 2019). In many of these applications such as high-performance structural materials, the importance of the fundamental insights offered by detailed mechanics based studies (Meng and Wang 2019; Chen et al. 2020; Ray et al. 2020) is paramount.

To address the structure-performance relation of cellulose materials from a bottom-up perspective where experimental characterization is difficult, molecular dynamics (MD) simulations are extensively used to study in the nanoscale and envision macroscale predictions (Wu et al. 2013, 2014; Sinko et al. 2014; Sinko and Keten 2015; Xia et al. 2018). A recent study (Zhu et al. 2015) uses MD simulations to reveal that the anomalous but desirable scaling law of simultaneous increase of the two conflicting mechanical properties of cellulose nanopaper (i.e., strength and toughness) is due to the facile breaking and reformation of hydrogen bonds between the neighboring molecular cellulose chains. In separate studies, MD simulations have complemented experiments to shed mechanistic insights on various material systems such as oxidized wood fibers (Fang et al. 2014), cellulose/carbon nanotube macrofibers (Li et al. 2017), cellulose/graphene-oxide microfibers (Li et al. 2015), bacterial cellulose microfibers (Wang et al. 2017, 2018), wood films (Zhu et al. 2017) and cellulose-graphite composites (Zhou et al. 2019). However, in spite of the advantages against experimental characterization, there are limitations in using MD simulations as a modeling tool.

MD simulations, usually effective at the nanometer length scale and at the time scale up to nanoseconds, are severely restricted to model material systems at the length scale comparable to experimental specimen because of the prohibitive computational expenses. Hence coarse-grained (CG) modeling schemes are desirable to bridge the gap between the nanoscale properties with the continuum (Fan and Maranas 2015; Song et al. 2018b). Several CG models with variable mapping degrees have been developed in the past for mechanics studies, such as predicting strategies for improving the mechanical strength of cellulose nanopapers (Qin et al. 2017) or capturing the elastic properties of the cellulose nanocrystals (Shishehbor and Zavattieri 2019). But these existing CG models are either unable to differentiate between smaller nanofibrils and larger microfibers or may not be able to model random network of cellulose probably due to modeling approximations. Another study (Mehandzhiyski et al. 2020) uses a non-scalable CG scheme to model a highly porous percolative network representative of cellulose based hydrogels. This model captures the value of elastic modulus for a single cellulose fibril close to experiments but the reported strength of fibrils ($\sim$700 MPa) is order of magnitudes lower than the previous estimated fibril strength of 6-10 GPa (Ahmed et al. 2005; Saito et al. 2013). Other random network modeling for cellulose based systems (Isaksson and Hägglund 2009; Mao et al. 2017; Goutianos et al. 2018) uses finite element modeling (FEM) at continuum length scales, which cannot consider the interactions among cellulose fibers, the key to understanding the deformation behaviors of cellulose based materials. Hence, a CG modeling scheme of cellulose materials to study the deformation and failure mechanism of cellulose-based materials with insight of the interplay among cellulose building blocks at different length scales, starting from molecular chain, to nanofiber, and finally to microfiber scales is essential.

Here, we present a bottom-up, scalable CG scheme based on atomistically informed MD simulations to study the response of cellulose fibers under various representative loading, such as shearing and opening. In addition, we devise a random network model of cellulose fibers, mimicking cellulose nanopaper as fabricated in experiments, and demonstrate the relation of strength and stiffness with respect to various cellulose fiber lengths. The depiction of cellulose film fracture, otherwise impossible by lower-level atomistic MD simulations, can also be effectively captured by the CG simulations. Our scalable CG scheme consists of three levels, ranging from Level-1 (smallest fiber diameter), Level-2 to Level-3

(maximum fiber diameter). The present CG model has the scope to be extended to further complex material systems, such as hybrid cellulose fibers having variable diameters by using (Wang et al. 2020) different CG beads at Level-1, Level-2 and Level-3 as the fundamental building blocks. The potential energy of constructed fibers can be obtained as $E(new) = \sqrt{E(a) \times E(b)}$, through the customary Lorentz-Berthelot mixing rules (Boda and Henderson 2008), where $E(a)$ and $E(b)$ are the potentials obtained in any two stages of Level-1, Level-2 or Level-3. Thus the developed CG model presents multifaceted opportunities in the mechanics design of novel cellulose based materials.

## A bottom-up, scalable CG modeling scheme of cellulose materials

The CG modeling scheme starting from one molecular chain of cellulose and using data from atomistic simulations is devised step by step to scale up to lengths reaching micrometers. To design the first level of the CG model (Fig. 1a), referred to as Level-1 CG hereafter, we represent the assembly of 21 carbon, oxygen and hydrogen atoms present in one anhydroglucose monomer ($C_6H_{10}O_5$) unit of a molecular cellulose chain by a single CG bead. This bead is chosen so as to minimize the risk of artifical reduction of conformational degrees of freedom due to its much softer torsion potential (Fan and Maranas 2015). To evaluate the equilibrium bond length ($R_o$) (Fig. 1b), bond angle ($\theta_o$ (Fig. 1c) and the dihedral angle ($\Phi_o$) (Fig. 1d) between the Level-1 CG beads, we construct three separate atomistic models consisting of 2, 3 and 4 glucose units of cellulose, respectively, in a water simulation box (Fan and Maranas 2015) with dimensions of 36 Å by 20 Å by 20 Å. The initial parametrization (Level-1) of the CG model thus takes into account the effect of bound water. After model relaxation using the conjugate gradient algorithm to minimize the total energy of the system until the total atomic forces are less than $10^{-10}$ eV/Å, we apply canonical ensemble (NVT) at 300K to equilibrate the system with time and calculate the center of mass (Izvekov and Voth 2005) of each glucose unit from the atomic trajectories. Each of the bond length ($R$), bond angle ($\theta$) and dihedral angle ($\Phi$) terms are obtained as the system evolves with time towards equilibration, by averaging 50 trajectories of an equilibrated configuration, for each of Fig 1b–d. The bond length, bond angle and dihedral angle data obtained from these all-atom simulations were then superposed to represent the bonded interactions of the Level-1 CG model. When each curve stabilizes (Fig. 1b–d), we obtain the equilibrium parameters of $R_o$ (0.546 nm), $\theta o$ (163.27°) and $\Phi_o$ (171.42°). Timestep in our simulations is set as 0.25 fs. A larger timestep is expected to yield coincidental results of the elastic region in the stress-strain plot but can mitigate the important features of oscillations in the plot and thus avoided here (Rouhi 2019).We employ the REAX potential (Mattsson et al. 2010) known to effectively capture force interactions in cellulose models to run our simulations.

The bonded interactions ($U_{bond}$) in a molecular chain to incorporate the stretching, bending and twisting (Ogawa 2019) is captured by three terms: two-body bond energy term, three-body angle energy term and the four-body dihedral energy term:

$$U_{bond} = \sum k_{bond}(R - R_o)^2 + \sum k_{angle}(\theta - \theta_o)^2 + \sum k_{dihed}(1 + \cos(\Phi - \Phi_0)) \quad (1)$$

To compute each bonded force parameter ($k_{bond}$, $k_{angle}$ and $k_{dihed}$), we stretch, bend and apply torsion to atomistic single cellulose chain models with 2, 3 and 4 glucose units, respectively, and compare the potential energies of the atomistic models with the corresponding analytical equation (1) representing the Level-1 CG model. The force acting on one Level-1 CG bead is matched with the reference forces, as proposed by (Izvekov and Voth 2005), acting on 21 carbon, oxygen and hydrogen atoms obtained from atomistic simulations. The CG bonded parameters are evaluated as $k_{bond}$ = 90.283 kcal mole$^{-1}$Å$^{-2}$, $k_{angle}$ =111.5109 kcal mole$^{-1}$ deg$^{-2}$ and $k_{dihed}$ =8.409 kcal mole$^{-1}$, which compare well with previous literature literature ($k_{bond}$ = 89.86 kcal mole$^{-1}$Å$^{-2}$, $k_{angle}$ =106 kcal mole$^{-1}$ deg$^{-2}$ as in (Fan and Maranas 2015). We model the non-bonded interactions between beads of the adjacent chains ($U_{inter}$) by

$$U_{inter} = 4u_{o\_inter}\left[(r_{o\_inter}/r)^9 - (r_{o\_inter}/r)^6\right], \quad (2)$$

where $r$ is the separation distance between the beads at any given time, and the non-bonded energy parameters $u_{o\_inter}$ and $r_{o\_inter}$ characterize the depth of the

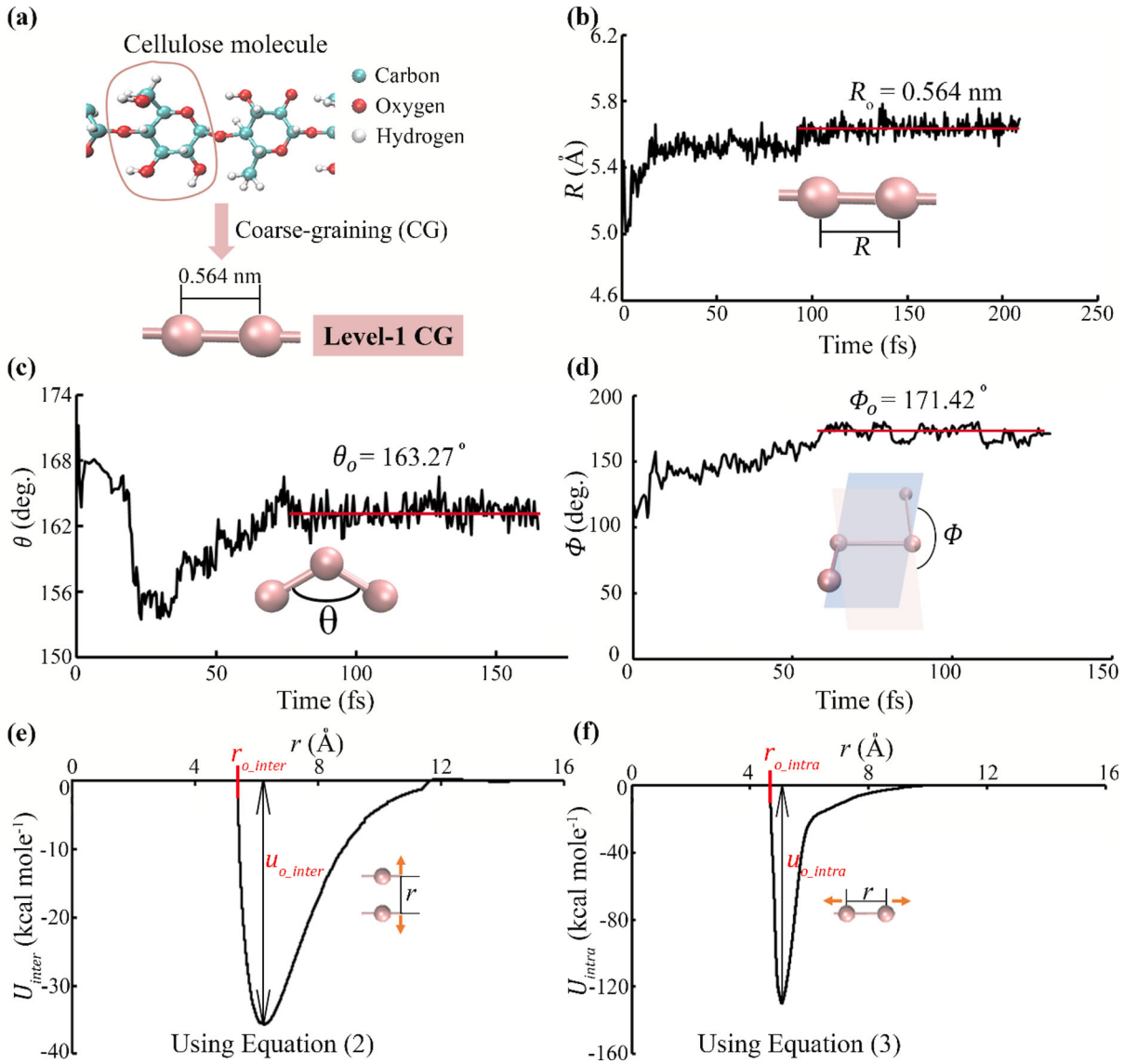


**Fig. 1** **a** Level-1 CG scheme. Each glucose unit of the molecular cellulose chain is mapped as one Level-1 CG bead of cellulose. **b–d** Evolution of the **b** bond length ($R$), **c** bond angle ($\theta$) and **d** dihedral angle ($\Phi$) versus time (fs) obtained from atomistic simulations. The equilibrated bond length $R_o$, bond angle $\theta_o$ and dihedral angle $\Phi_o$, are computed as 0.546 nm, 163.27° and 171.42°, respectively. **e** Plot of non-bonded interaction energy between beads of neighboring chains $U_{inter}$ (kcal/mole) versus the distance of separation ($r$) of the beads for evaluation of the non-bonded parameters for Level-1 of the CG scheme. **f** Plot of non-bonded interaction energy between beads of the same chain $U_{intra}$ (kcal/mole) versus the distance of separation ($r$) of the beads for evaluation of the non-bonded parameters for Level-1 of the CG scheme

potential well and the equilibrium position of the pair potential, respectively, which are derived from the explicit hydrogen bond energy term of the REAX potential at the atomistic level. Equation (2) is known to capture non-bonded interactions (Srinivas et al. 2011), designated by wider potential wells, between neighboring chains. Furthermore, we represent the non-bonded interactions between beads in the same chain ($U_{intra}$) by

$$U_{intra} = 4u_{o\_intra}\left[(r_{o\_intra}/r)^{12} - (r_{o\_intra}/r)^{6}\right], \quad (3)$$

where $u_{o\_intra}$ and $r_{o\_intra}$ are of similar meaning as $u_{o\_inter}$ and $r_{o\_inter}$, respectively. To evaluate $U_{inter}$ and

$U_{intra}$, we vary the distance between two glucose units representing two CG beads to obtain the non-bonded interaction energies relative to the separation distance $r$ as shown in Fig. 1e and 1f, respectively, and then calculate the non-bonded parameters ($u_{o\_inter}$ and $r_{o\_inter}$, $u_{o\_intra}$ and $r_{o\_intra}$) by curve fitting as shown in Fig. 1e–f.

For representing the Level-2 CG scheme (Fig. 2a), we construct a model that comprises of 36 Level-1 beaded chains based on the crystalline structure of cellulose 1β, most commonly found in plants (Moon et al. 2011a). Each chain contains 6 Level-1 CG beads. The CG bead length for Level-2 is ∼3.384 nm. To evaluate the bonded force parameters of the Level-2 from Level-1, we assume periodic conditions so that each bead is connected to two other beads on its two sides. Also, since the cellulose structures show self-similarity in one direction (self-affine) (Redinz and Guimarães 1997; Fan et al. 1999; Buzio et al. 2004; Koňas et al. 2009), we use the techniques of comparing the parametric bonded force parameter equations of corresponding CG levels for scaling up as used in previous other literatures (Zhu et al. 2014b). For example, since 36 chains each comprising of six beads form one bead of the Level-2, the equation of bond energy of two connected beads of Level-2 (*L2*) is given by

$$U_{bond\_L2} = k_{bond\_L2} b_{i+1} c_{i+1} [6(R - R_o)]^2 \quad (4)$$

where $b_{i+1}$ and $c_{i+1}$stands for the number of bonds and chains, respectively, formed at CG Level-($i$+1). When $i$=1, it represents parameters from Level-1 and hence ($i$ + 1) denotes parameters of Level-2. From our calculations, $b_{i+1}$= 2 and $c_{i+1}$= 1. The bond energy equation of the corresponding Level-1 (*L1*) beads is given by

$$U_{bond\_L1} = k_{bond\_L1} b_i c_i [(R - R_o)]^2 \quad (5)$$

where $b_i$ = 12 and $c_i$= 36 represents the number of bonds and chains, respectively, formed by Level-1 CG beads, respectively, to scale up to the CG Level-2. Comparing the equations (4) and (5) ($U_{bond\_L2} = U_{bond\_L1}$), we have

$$k_{bond\_L2} = 6k_{bond\_L1} \quad (6)$$

The angle energy term of the corresponding Level-1 beads forming three Level-2 CG beads is given by

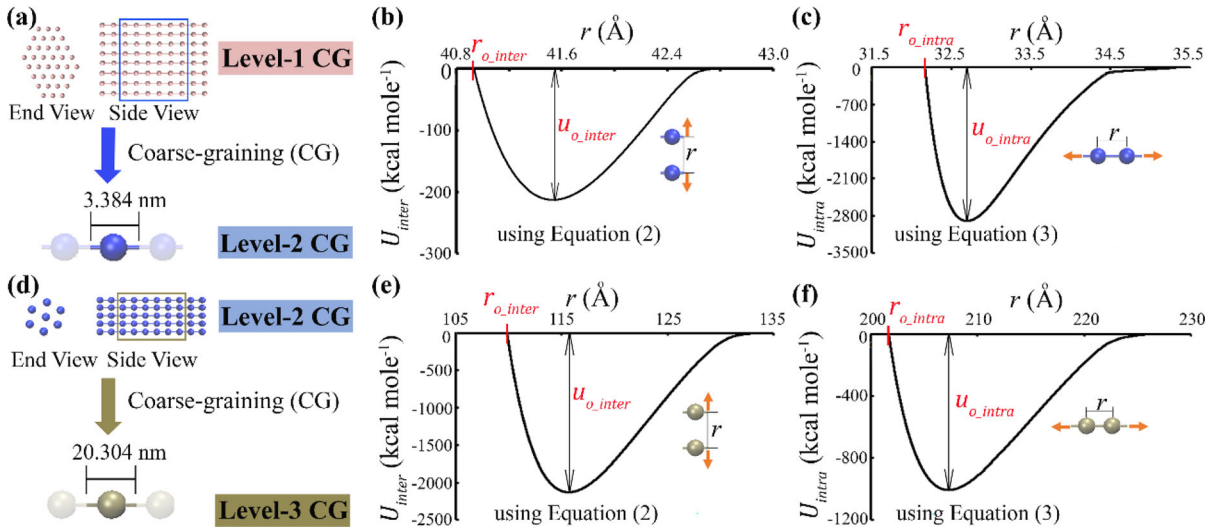


**Fig. 2** **a** Level-2 CG scheme. Here, 36 chains, each comprising of six Level-1 CG beads are mapped to form one Level-2 CG bead as shown in the schematic. The bond length between two Level-2 CG beads is 3.384 nm. **b–c** Plots of non-bonded vdW interaction energy **b** between beads of the adjacent chains $U_{inter}$ (kcal/mole) and **c** between beads of the same chain $U_{intra}$ (kcal/mole) versus the distance of separation ($r$) of the beads for evaluation of the non-bonded parameters ($r_o$and $U_o$) for Level-2 of the CG scheme. **d** Level-3 CG scheme. Here, 7 chains, each comprising of six Level-2 CG beads are mapped to form one Level-3 CG bead as shown in the schematic. The bond length between two Level-2 CG beads is 20.304 nm. **e–f** Plots of vdW interaction energy with **e** neighboring beads of different chains $U_{inter}$ (kcal/mole) and **f** adjacent beads of the same chain $U_{intra}$ (kcal/mole) versus the distance of separation ($r$) of the beads for evaluation of the non-bonded parameters for Level-3 of the CG scheme

$$U_{angle\_L1} = k_{angle\_L1} b_i c_i (\theta - \theta_o)^2 \quad (7)$$

where $b_i = 18$ represents the number of bonds from beads and $c_i = 36$. The corresponding angle energy term of the Level-2 beads is given by

$$U_{angle\_L2} = k_{angle\_L2} b_{i+1} c_{i+1} (\theta - \theta_o)^2 \quad (8)$$

where $b_{i+1} = 3$ and $c_{i+1} = 1$ represents the number of bonds and chains, respectively, formed by Level-2 beads. Comparing (7) and (8), we get

$$k_{angle\_L2} = 216 k_{angle\_L1} \quad (9)$$

Similarly, comparing the two dihedral energy terms, we obtain

$$k_{dihed\_L2} = 216 k_{dihed\_L1} \quad (10)$$

To evaluate the non-bonded interactions between different ($U_{inter}$) and same chains ($U_{intra}$), the Level-1 structures as shown in Fig. 2a are energy minimized and equilibrated following similar procedure as before and then modeled as rigid bodies to restrict the natural twisting of the cellulose bundle (Ogawa 2019). The non-bonded force parameters ($U_{inter}$) and ($U_{intra}$) are evaluated by fitting the corresponding energy versus separation distance curve as shown in Fig. 2b, c, respectively, to obtain the non-bonded force parameters $u_{o\_inter}$, $r_{o\_inter}$, $u_{o\_intra}$ and $r_{o\_intra}$. It is to be noted that the structure in Fig. 2a has a non-symmetric hexagonal shape with three different interfaces. The non-bonded interaction energies per unit area relative to the separation distance $r$, across three different interfaces are computed (Fig. S1 in supplementary information). The magnitudes of the normalized potential well in the three plots are observed to be almost identical. This suggests that non-bonded interaction energies per unit bead are relatively constant irrespective of the interface. Hence, the maximum inter-bead distance bound is used here to parametrize non-bonded interaction energy while scaling up from Level-1 to Level-2. This is a reasonable choice to avoid the overlap of the fibers at higher levels of the developed CG scheme and thereby simplifying the modeling scheme without loss of generality.

For Level-3 CG (Fig. 2d), we construct the beads of crystalline cellulose with 7 Level-2 beaded chains, each containing 6 Level-2 beads, to model a micron-scale cellulose fibril having a diameter of 10.98 nm, in accordance with experimental observations ($\sim$ 10-15 nm as in (Zhu et al. 2014a)(Szymanska-Chargot et al. 2017). The CG bead length for Level-3 is $\sim$20.304 nm. We use similar procedure as in Level-2 to compute the bonded force parameters for Level-3 (*L3*). For denoting parameters of *L3*, the subscript ($i$+2) is used following the usual notations as before. Here, we obtain

$$k_{bond\_L3} = 7/6 k_{bond\_L2} \quad (11)$$

Similarly, the angle parameter at Level-3 is calculated

$$k_{angle\_L3} = 42 k_{angle\_L2} \quad (12)$$

Also, the dihedral parameter at Level-3 is calculated following the same equation and is represented as

$$k_{dihed\_L3} = 42 k_{dihed\_L2} \quad (13)$$

The non-bonded interactions between different ($U_{inter}$) and same chains ($U_{intra}$) are evaluated by fitting the corresponding energy versus separation distance curve of Level-2 beads forming corresponding Level-3 beads as shown in Fig. 2e–f, respectively, to obtain the non-bonded force parameters of Level-3. We carry the CG simulations in LAMMPS (Plimpton 1995). All CG force field parameters values evaluated across Level-1 to Level-3 are listed in Table 1.

## Results and discussion

To validate our CG modeling scheme, we compare the Level-1 CG model, comprising of beads as described in Fig. 1a with full atomistic modeling (AM). Here, a cellulose bundle with seven molecular chains, each having 8 repeat units (8 glucose monomer units) and length 4.38 Å as shown in Fig. 3a (top panel). An equivalent Level-1 CG model consisting of 7 chains, each containing 8 repeat units (Level-1 beads) is also constructed (Fig. 3a, bottom panel). The models are energy minimized first (Fig. S2 in supplementary information) before carrying out the simulations using microcanonical (NVE) ensemble to make the conditions comparable with the all-atomistic model used in the reference (Zhu et al. 2015). The simulations mimic inter-fiber sliding of the cellulose chains in the fiber bundle and the middle chain (inset of Fig. 3a) is pulled out. We compare the variation of total potential energy (Fig. 3b) during the sliding process for the above two (AM and CG) simulation models. The results from the

**Table 1** CG force field potential parameters

| | Level-1 | Level-2 | Level-3 |
|---|---|---|---|
| $R_O$ | 0.564 nm | 3.384 nm | 20.304 nm |
| $k_{bond}$ | 90.28 kcal mole$^{-1}$Å$^{-2}$ | 541.69 kcal mole Å$^{-1}$Å$^{-2}$ | 631.98 kcal mole$^{-1}$Å$^{-2}$ |
| $k_{angle}$ | 111.51 kcal mole$^{-1}$ deg$^{-2}$ | 24086.35 kcal mole$^{-1}$ deg$^{-2}$ | 1011626.88 kcal mole$^{-1}$ deg$^{-2}$ |
| $k_{dihed}$ | 8.41 kcal mole$^{-1}$ | 1816.34 kcal mole$^{-1}$ | 76286.45 kcal mole$^{-1}$ |
| $u_{o\_intra}$ | 129.10 kcal mole$^{-1}$ | 2895.42 kcal mole$^{-1}$ | 1004.87 kcal mole$^{-1}$ |
| $r_{o\_intra}$ | 0.47 nm | 3.22 nm | 20.17 nm |
| $u_{o\_inter}$ | 34.77 kcal mole$^{-1}$ | 212.97 kcal mole$^{-1}$ | 2128.43 kcal mole$^{-1}$ |
| $r_{o\_inter}$ | 0.537 nm | 4.093 nm | 10.983 nm |

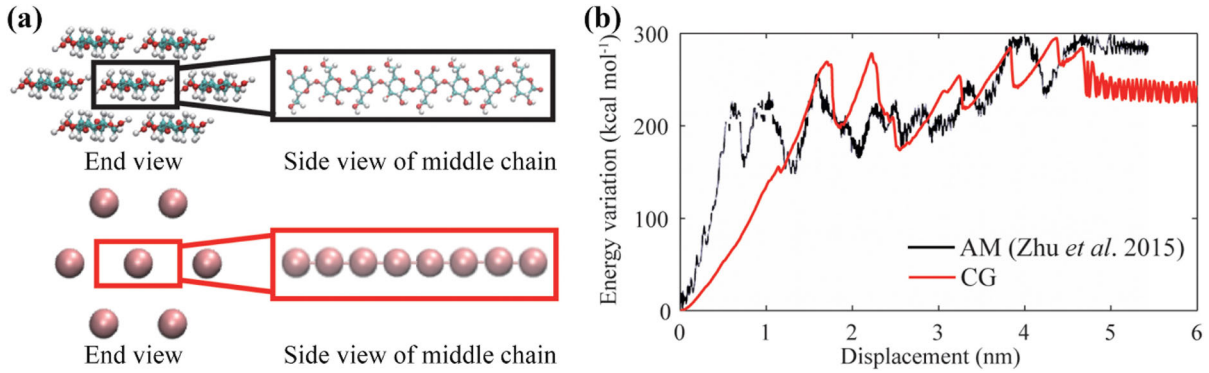


**Fig. 3** Validation of the Level-1 CG model with an atomistic model (AM) from previous literature (Zhu et al. 2015). Here, the atomistic model consists of seven molecular cellulose chains, each having 4 repeat units (eight glucose units, as illustrated in the zoom-in view). The middle chain is pulled out of the surrounding six neighboring chains. To verify our scheme, we build an analogous CG based model to mimic the pulling out simulation. The potential energy variation (kcal mole$^{-1}$) with respect to the pulling displacement (nm) is plotted and the energy variation matches well with the atomistic simulation results for ref. (Zhu et al. 2015)

AM model are obtained from Ref. (Zhu et al. 2015). The pulling is initiated by applying a velocity of 0.001Å/fs in the first glucose unit and the first CG bead of the AM and CG models, respectively. The initial increase of both curves results from the tension of cellulose chains. At the initial stages of pulling out of middle chain in the CG simulations, the applied tension is transferred stepwise starting at the pulled end and slowly transmitted to the other end of the chain. During the initial stages before the advent of inter-fiber sliding, the energy variation in the CG simulations is captured by the bond energy incorporated within equation (1). This equation developed using the coarse-graining methodology is an approximated form of the bond energy described by the REAX potential, developed using first principle calculations in atomistic simulations. The lag in the energy variation curve obtained through CG modeling is mainly because of the energy drop due to the approximations while formulating the CG scheme. When the whole chain slides, both curves of the energy variation versus pulling displacement feature the zigzag nature, indicating the cascade of hydrogen bond forming (curve rise till the local peak), breaking (curve drop from local peak to local trough) and reforming (curve rising from the trough to the next peak), a representative feature of the relative sliding between cellulose chains. The similar tendency and amplitude of the zigzags in both curves show that the CG model is accurate enough to the parameterization of bond and non-bond interaction. The maximum amplitude of the CG model (corresponding to displacement $\sim$ 1.5–4.8 nm) is within 1.6% tolerance to that predicted by the atomistic model. Since the

maximum energy dissipated while sliding is an indicator of the extent of breaking and reformation of the hydrogen bonds before final failure, the accuracy of median energy and amplitude of curve suggests that the developed CG model can effectively capture the failure modes in cellulose fibers. This proves that our CG model can capture reasonably well the hydrogen bond breaking and reforming of the molecular cellulose, a deformation mechanism dissipating a significant proportion of energy while the cellulose fibers are undergoing interfacial sliding.

Figure 4 plots the mechanical response of the cellulose fibers under two representative loadings such as shearing and opening. In shearing loading, two fibers, each 1.22 μm long, comprised of 60 Level-3 CG beads, slide (red arrows in Fig. 4a) against each other parallel while in opening loading, the same two fibers are opened by pulling the left most beads (red arrows in Fig. 4c) away from each other. For the shearing mode, the pulling is initiated by applying a velocity of 0.0001Å/fs to the end beads. The temperature is controlled around 5K to reduce the thermal noise while undergoing shearing. For the opening mode, fibers are separated by applying a velocity of 0.0001Å/fs to the leftmost beads (red arrows in Fig. 4c). The other ends of the fibers undergoing deformation by opening are allowed motion only along x- and y-direction (wiggly lines in Fig. 4c schematic) to execute pure opening deformation modes in our model. Both the shearing and opening simulations are performed under microcanonical ensemble with a timestep of 0.25 fs and the energy data points are collected after every 5000 timesteps. For both deformation modes, we plot the average the averaged potential energy (kcal mole$^{-1}$) versus the pulling displacement (microns) (Fig. 4a, b).

The energy variation versus pulling displacement plot (Fig. 4a) of the shearing simulation shows an

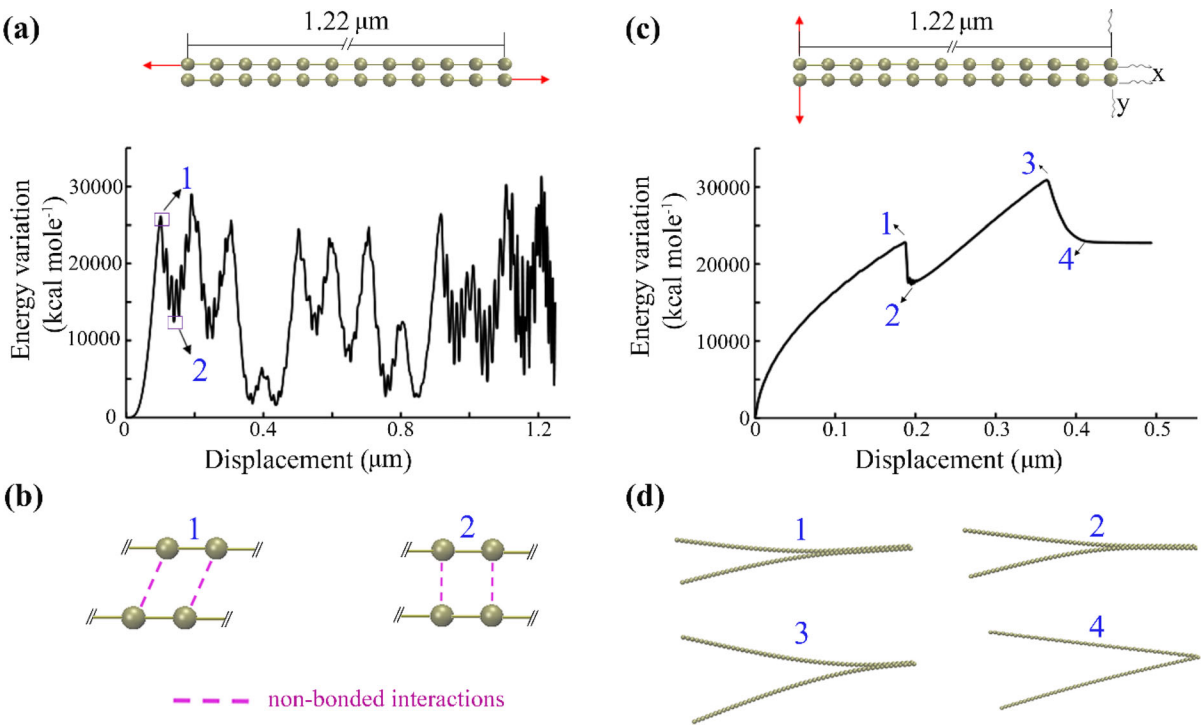


**Fig. 4** Simulations of shearing and opening between two fiber models built using Level-3 beads from the devised CG scheme. Each of the two fibers have length 1.22 μm. **a** Potential energy variation (kcal mole$^{-1}$) versus the pulling displacement (μm) as the fibers slide relative to each other, indicating shearing. **b** Schematic showing the beads under shearing deformation causing the peaks (first peak labelled 1 in blue) and troughs (first trough labelled 2 in blue) of **a**. **c** Potential energy variation (kcal mole$^{-1}$) versus the opening displacement (μm) as the fibers bend relative to each other. **d** Snapshots of the bending deformation corresponding to the peaks and troughs (labelled 1, 2, 3 and 4 in blue) of **c**. The directions of shearing and opening are indicated by red arrows

initial linear profile symbolizing immense bending of the chains initially starting to slide relative to each other. This is accompanied by non-bonded interactions between one bead of the first chain and the adjacent bead of the neighboring chain. As the resistive force imposed by the non-bonded energy between the beads of the neighboring chains trying to restrict the shearing increases, the beads are stretched to the maximum extent as shown in Fig. 4b (labelled 1 in blue) corresponding to the first peak of Fig. 4a (labelled 1). As the shearing continues, the same bead reaches an equilibrium position (local minima) by aligning itself with the next bead of the neighboring chain as depicted by the schematic corresponding to the first trough (labelled 2 in Fig. 4b). This stretching of beads of adjacent chains followed by energy stabilization continues with further progress of shearing resulting in the zigzag amplitude of the energy profile. The curvy nature stems from the hydrogen bonding originating from the molecular level cellulose chains. The facile breaking and reformation of hydrogen bonds cause resistance to the sliding chains, which results in tremendous dissipation of energy. The cascading effects of strong inter-fiber non-bonded energy continue until the whole chain is pulled out, which indicates failure.

Figure 4c shows the energy profile of two fibers opening relatively to each other. Here, in the first part of the potential energy variation versus the pulling displacement (displacement from 0 to 0.175 μm), the fibers bend and move away from each other while trying to resist the opening deformation. The simulation snapshot (labelled as 1 in Fig. 4d) demonstrates the initial phase of the bending process corresponding to the first peak of the energy profile (Fig. 4c). As further opening is imposed, there is a steep drop in the energy profile. It is mainly because the remaining part cannot resist the bending and relax the potential energy suddenly by partial separation (corresponding to the label 2 of Fig. 4d) and adjusting their orientation (right end of snapshot 2 (Fig. 4d) goes down). With the further increase of opening deformation, the energy profile rises again until it reaches a global maximum in the energy profile (labelled as 3 in Fig. 4d), corresponding to the further bending. When the remaining part cannot maintain the bending again, the curve drops suddenly drops suddenly due to stopping of the bending and release of energy as the fibers straightened (snapshot 4 in Fig. 4d). Due to the length of fiber in our simulations, such an energy variation appears twice until the two chains completely separate from each other (labelled as 4 in Fig. 4d).

Furthermore, the CG modeling scheme is applied to study the mechanical properties of a random network of cellulose fibers, which is a reasonable estimate of the material structure of cellulose nanopaper in experiments (Zhu et al. 2015). Such a simulation is crucial for revealing the deformation and failure mechanisms of cellulose nanopaper that are challenging and/or impossible to capture in experiments, and also cost prohibitive for fully atomic simulations. To investigate the effect of cellulose fiber length on the mechanical properties of cellulose nanopaper, three random network models with an fiber length of 0.9 μm, 1.2 μm and 1.5 μm, respectively, are constructed. The total number of Level-3 CG beads in each of the three models are is 29,508 (± 0.005% tolerance) corresponding to 267,696,576 atoms. Fully atomistic simulations of such a model size are prohibitive. Experimental tensile tests are usually performed by cutting thin strips of specimens from the bulk sample which may result in broken fibers at the edges. To accurately reproduce the experiments, randomly oriented fibers are placed into a simulation box of size 6 μm by 1.5 μm by 0.1 μm and fibers are cut if they protrude the simulation box. The minimum length of the remaining small fiber is set to be larger than 0.1 μm for the convergence of simulations. Each CG model is relaxed using the conjugate gradient algorithm to minimize the total energy of the system by decreasing the total atomic forces less than $10^{-15}$ eV/Å, thus releasing the internal stress sufficiently. After a relaxation with canonical ensemble, the left and right ends ($\sim$1.5 μm from each end) are set as rigid bodies to incorporate the effect of clamps in a tensile testing machine. Uniaxial tension is applied by pulling the right end (red arrows in Fig. 5a) at a constant velocity of 0.001 Å/fs using a timestep of 0.25 fs under microcanonical ensemble, while the other (left) end is kept fixed. Stress is calculated by computing the sum of stress components of the mobile segment of the model along the tensile loading direction.

Figure 5a shows the deformation of one model of randomly distributed cellulose fiber network where the maximum length of each fiber is 1.2 μm. The initial structure before application of tensile loading (strain = 0%) is shown in Fig. 5a (top panel). The random

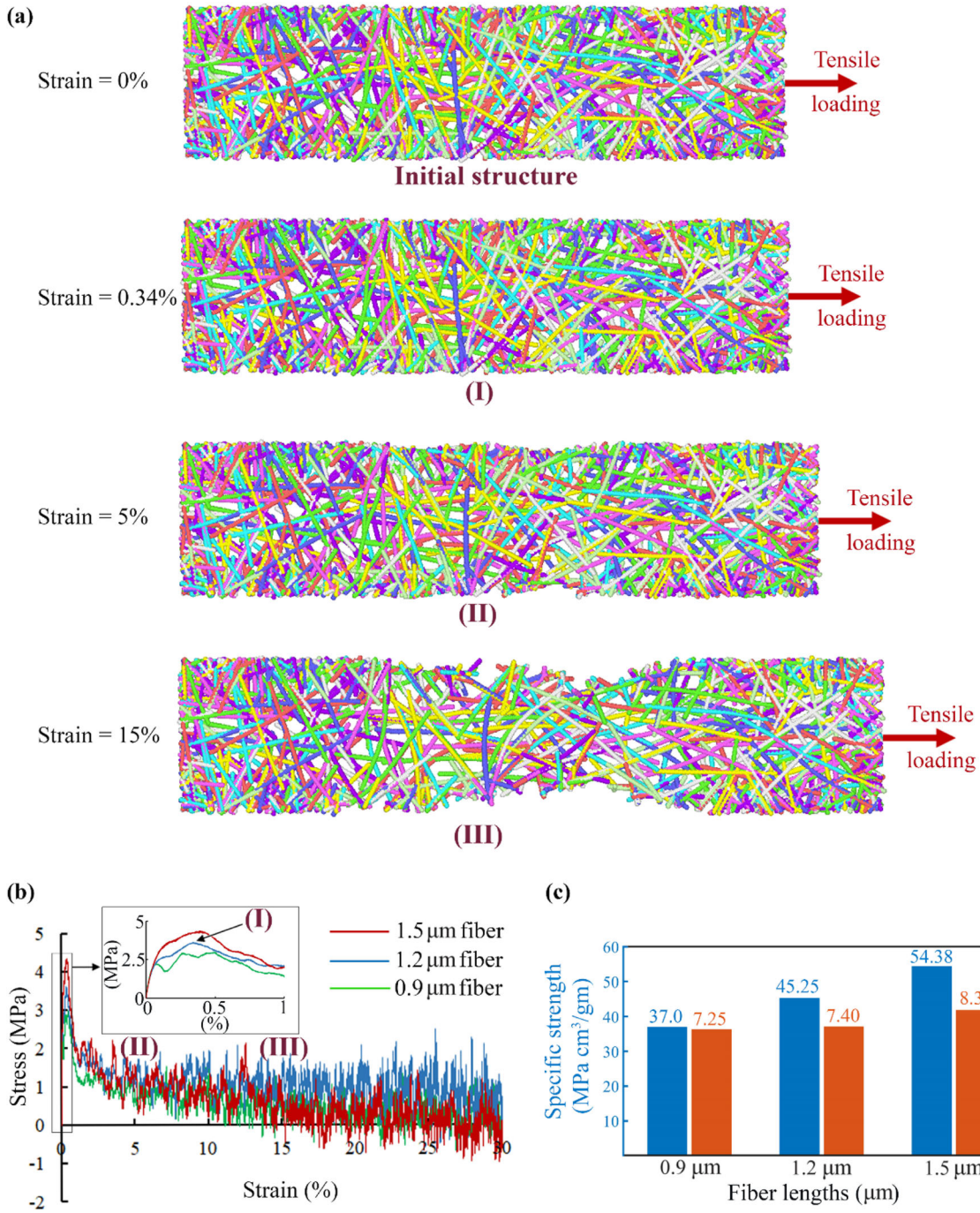


**Fig. 5** CG modeling and mechanical behavior of cellulose nanopaper films. **a** Deformation snapshots of a random network of cellulose fibers made of Level-3 CG beads. The deformation snapshots of the model, consisting of fibers having a maximum length of 1.2 μm fiber, under tension (red arrows) is shown here. The initial structure before deformation is shown in the top panel. The snapshots corresponding to variable strains of 0.34%, 5% and 10% are labeled (I), (II) and (III), respectively. **b** Engineering stress (MPa) versus the strain (%) plots for the random networks with different fiber lengths: 0.9 μm (green), 1.2 μm (blue) and 1.5 μm (red). Inset shows the magnified stress-strain plots at strains ranging from 0 to 1% to display clearly the peak stress values for the three models. **c** Comparisons of the specific strength (MPa $cm^3$/gm) and stiffness (GPa) for all three models with varying fiber lengths (0.9 μm, 1.2 μm and 1.5 μm)

network is modeled on the hypothesis that thicker cellulose fibers with the diameter in the range of 10–20 nm, as present in the current CG model, are relatively shorter and straight, as evidenced by experimental characterization in separate investigations (Usov et al. 2015). Three deformation snapshots of the model under tensile loading are labeled (I), (II) and (III) in Fig. 5a, corresponding to strains of 0.34%, 5% and 15%, respectively. When uniaxial tension is applied, the randomly oriented cellulose fibers start to slide apart from each other and non-bonded interactions, mainly arising from hydrogen bonding among the neighboring fibers, resist the sliding in between the cellulose fibers until the stress-strain plot reach the global maximum (label I). As the tensile strain increases, the celloluse nanopaper elongates in tensile direction and contracts in the perpendicular direction, until cracks initiate at the edges which lead to stress concentration and thus localized deformation in the nanopaper (label II). Upon further tensile loading, the localized deformation causes the cellulose fibers in the severely deformed region to be more aligned with the tensile direction. The failure of the cellulose nanopaper occurs when the cellulose fibers slide off from each other in the localized deformation region (see supplemental videos). It is to be noted that no breakage of cellulose fibers is observed in the simulations, which asserts on the understanding that failure in cellulose nanopaper is mainly due to inter-fiber sliding instead of individual cellulose fiber fracture, largely due to the superb mechanical properties of individual fibers (up to 7.5 GPa of tensile strength) (Domingues et al. 2014). Similar deformation and failure behaviors are also observed in the other two sets of CG modeling, with a cellulose fiber length of 0.9 μm and 1.5 μm, respectively. The simulation videos for the three models are shown in the electronic supplementary information.

Figure 5b plots the stress-strain curves of the three models obtained from CG simulations, from which the tensile strength and stiffness of the corresponding cellulose nanopapers can be determined, as compared in Fig. 5c. The specific strength of the cellulose nanopaper increases as the cellulose fiber length increases, e.g., 37.0 MPa $cm^3$/gm, 45.25 MPa $cm^3$/gm, 54.38 MPa $cm^3$/gm, for fiber length of 0.9 μm, 1.2 μm and 1.5 μm, respectively. It is acknowledged that a fair comparison is difficult because of the diverse processing conditions to fabricate the cellulose nanopaper and hence, a clear illustration noting the different fiber lengths as well as fiber diameters of various experimental samples is included in Table S1 of the Supplementary Information. Our specific strength values (37.0–54.38 MPa $cm^3$/gm) agree reasonably well with some previous literature (Sehaqui et al. 2011; Yousefi et al. 2013; Motamedian et al. 2019). Such a fiber length dependence of tensile strength of cellulose paper can be attributed to the fact that increasing degree of polymerization or length of a cellulose fiber allows for more non-bonded interactions between neighboring cellulose fibers, which in turn lead to higher energy dissipation during the tensile deformation and failure of the cellulose nanopaper. In other words, longer cellulose fibers can resist more tensile deformation as a higher energy is required to fail the random network of cellulose fibers, which corresponds to a higher tensile strength with increasing cellulose fiber length. This is well aligned with previous multi-scale crack bridging models which emphasize that the absence of hydrogen bonding is the primary factor in reducing the fracture toughness drastically, thus leading to accelerated failure in the cellulose nanopaper (Meng et al. 2017). The oscillation of the stress-strain curves after the tensile stress peaks results from the cascade of events of hydrogen bond formation, breaking and reformation, as the cellulose fibers in the nanopaper model slide relative to each other with the increase in the tensile strain. Such oscillations from positive to negative stress values at large strains ($\sim$12-30%) can be observed in studies related to atomistic and coarse-grained models (Wu et al. 2014)(Shishehbor and Zavattieri 2019)(Sinko and Keten 2015) but hard to be observed in the experimental test samples, due to length scale effects. The stiffness of the cellulose nanopaper increases modestly as the cellulose fiber length increases, e.g., 7.25 GPa, 7.40 GPa, 8.35 GPa, for fiber length of 0.9 μm, 1.2 μm and 1.5 μm, respectively, which can be attributed to the higher non-bonded interactions (e.g., hydrogen bonds) between neighboring cellulose fibers. The range of stiffness of cellulose nanopapers is well in line with the experimental measurements ($\sim$ 7 to 11 GPa as in Table S1 in supplementary information) (Sehaqui et al. 2011; Zhu et al. 2015). The dependence of tensile strength and stiffness of cellulose nanopaper on the constituent cellulose fiber length revealed by the CG simulations can serve as a quantitative guideline for

designing cellulose nanopaper with desirable mechanical properties.

## Conclusions

In conclusion, we design a bottom-up, scalable CG scheme that enables modeling of cellulose fibers ranging from nanometers to microns at a low simulation cost, a much sought capability in understanding the deformation and failure mechanisms of cellulose nanopaper that is otherwise impossible by fully atomistic simulations. The CG scheme is validated by fully atomistic simulations and employed to investigate the behavior of cellulose fibers under representative mechanical loads. Furthermore, a random network of cellulose fibers in micron-scale in the plane under tensile deformation is simulated by CG scheme, a simulation task prohibitive for atomistic modeling. The CG simulation of such a random network of cellulose nanofibers offers crucial insights on the in situ deformation and failure mechanisms of cellulose nanopaper under tensile loading, which are challenging to observe in experiments. Parametric study using CG simulations reveals the dependence of tensile strength and stiffness of cellulose nanopaper on the length of constituent cellulose fiber, and offer quantitative design guidance of cellulose nanomaterials. The bottom-up and scalable nature of the CG scheme presented in this study might suggest its broader applicability in simulating cellulose-based materials with various feature sizes of material building blocks, which in turn may facilitate the design of cellulose materials with desirable mechanical properties. Incorporating additional functional groups as separate beads at Level-1 of the presented CG scheme to include the effects of other molecules such as hemicellulose and/or considering different ambient conditions (e.g. humidity (Hou et al. 2020)), and scaling it up till Level-3 may also form a basis for prospective research which may aid in analyzing mechanistic behavior of composite cellulose nanopapers and other cellulose based bulk structural materials (Guan et al. 2020), providing us the much needed guidance into design of cellulose based functional materials.

**Acknowledgements** We acknowledge the University of Maryland supercomputing resources (http://hpcc.umd.edu) and Maryland Advanced Research Computing Center (MARCC) made available for conducting the research reported in this paper. The authors acknowledge the support of US National Science Foundation (Grant Nos.1362256, 1936452).

**Compliance with ethical standards**

**Conflict of interest** The authors declare that they have no conflict of interest.

## References

Ahmed M, Azizi S, Alloin F, Dufresne A (2005) Review of recent research into cellulosic whiskers, their properties and their application in nanocomposite field. Biomacromolecules 6:612–626. https://doi.org/10.1021/bm0493685

Boda D, Henderson D (2008) The effects of deviations from Lorentz-Berthelot rules on the properties of a simple mixture. Mol Phys 106:2367–2370. https://doi.org/10.1080/00268970802471137

Buzio R, Calvini P, Ferroni A, Valbusa U (2004) Surface analysis of paper documents damaged by foxing. Appl Phys A Mater Sci Process 79:383–387. https://doi.org/10.1007/s00339-004-2540-2

Chen C, Kuang Y, Zhu S et al (2020) Structure–property–function relationships of natural and engineered wood. Nat Rev Mater. https://doi.org/10.1038/s41578-020-0195-z

Czaja WK, Young DJ, Kawecki M, Brown RM (2007) The future prospects of microbial cellulose in biomedical applications. Biomacromolecules 8:1–12. https://doi.org/10.1021/bm060620d

Diaz JA, Ye Z, Wu X et al (2014) Thermal conductivity in nanostructured films: from single cellulose nanocrystals to bulk films. Biomacromolecules 15:4096–4101. https://doi.org/10.1021/bm501131a

Domingues RMA, Gomes ME, Reis RL (2014) The potential of cellulose nanocrystals in tissue engineering strategies. Biomacromolecules 15:2327–2346. https://doi.org/10.1021/bm500524s

Dufresne A (2017) Cellulose nanomaterial reinforced polymer nanocomposites. Curr Opin Colloid Interface Sci 29:1–8. https://doi.org/10.1016/j.cocis.2017.01.004

Fan B, Maranas JK (2015) Coarse-grained simulation of cellulose Ib with application to long fibrils. Cellulose 22:31–44. https://doi.org/10.1007/s10570-014-0481-2

Fan K, Hatzikiriakos SG, Avramidis S (1999) Determination of the surface fractal dimension from sorption isotherms of five softwoods. Wood Sci Technol 33:139–149. https://doi.org/10.1007/s002260050105

Fang Z, Hou G, Chen C, Hu L (2019) Nanocellulose-based films and their emerging applications. Curr Opin Solid State Mater Sci 23:100764. https://doi.org/10.1016/j.cossms.2019.07.003

Fang Z, Zhu H, Yuan Y et al (2014) Novel nanostructured paper with ultrahigh transparency and ultrahigh haze for solar cells. Nano Lett 14:765–773. https://doi.org/10.1021/nl404101p

Goutianos S, Mao R, Peijs T (2018) Effect of inter-fibre bonding on the fracture of fibrous networks with strong interactions. Int J Solids Struct 136–137:271–278. https://doi.org/10.1016/j.ijsolstr.2017.12.020

Guan QF, Bin Yang H, Han ZM et al (2020) Lightweight, tough, and sustainable cellulose nanofiber-derived bulk structural materials with low thermal expansion coefficient. Sci Adv 6:1–9. https://doi.org/10.1126/sciadv.aaz1114

Hou Y, Guan Q, Xia J et al (2020) Strengthening and toughening hierarchical nanocellulose via humidity-mediated interface. ACS Nano. https://doi.org/10.1021/acsnano.0c08574

Ioelovich M (2008) Cellulose as a nanostructured polymer: a short review. BioResources 3(4):1403–1418

Isaksson P, Hägglund R (2009) Structural effects on deformation and fracture of random fiber networks and consequences on continuum models. Int J Solids Struct 46:2320–2329. https://doi.org/10.1016/j.ijsolstr.2009.01.027

Izvekov S, Voth GA (2005) A multiscale coarse-graining method for biomolecular systems. J Phys Chem B 109:2469–2473. https://doi.org/10.1021/jp044629q

Jia C, Chen C, Kuang Y et al (2018) From wood to textiles : top-down assembly of aligned cellulose nanofibers. Adv Mater 30:1801347. https://doi.org/10.1002/adma.201801347

Kalia S, Dufresne A, Cherian BM et al (2011) Cellulose-based bio- and nanocomposites: a review. Int J Polym Sci 2011:1–35. https://doi.org/10.1155/2011/837875

Klemm D, Heublein B, Fink H-P, Bohn A (2005) Cellulose: fascinating biopolymer and sustainable raw material Angewandte. Angew Chemie Int Ed 44:3358–3393. https://doi.org/10.1002/anie.200460587

Koňas P, Buchar J, Severa L (2009) Study of correlation between the fractal dimension of wood anatomy structure and impact energy. Eur J Mech A/Solids 28:545–550. https://doi.org/10.1016/j.euromechsol.2008.07.005

Li T, Zhai Y, He S et al (2019) A radiative cooling structural material. Science (80-) 364:760–763. https://doi.org/10.1126/science.aau9101

Li T, Zhu M, Yang Z et al (2016) Wood composite as an energy efficient building material : guided sunlight transmittance and effective thermal insulation. Adv Energy Mater 6:1601122. https://doi.org/10.1002/aenm.201601122

Li Y, Zhu H, Wang Y, Ray U et al (2017) Cellulose-nanofiber-enabled 3D printing of a carbon-nanotube microfiber network. Small Methods 1:1700222. https://doi.org/10.1002/smtd.201700222

Li Y, Zhu H, Zhu S et al (2015) Hybridizing wood cellulose and graphene oxide toward high-performance fibers. NPG Asia Mater 7:e150. https://doi.org/10.1038/am.2014.111

Mao R, Goutianos S, Tu W et al (2017) Modelling the elastic properties of cellulose nanopaper. Mater Des 126:183–189. https://doi.org/10.1016/j.matdes.2017.04.050

Mattsson TR, Lane JMD, Cochrane KR et al (2010) First-principles and classical molecular dynamics simulation of shocked polymers. Phys Rev B 81:054103. https://doi.org/10.1103/PhysRevB.81.054103

Mehandzhiyski AY, Rolland N, Garg M et al (2020) A novel supra coarse-grained model for cellulose. Cellulose 27:4221–4234. https://doi.org/10.1007/s10570-020-03068-y

Meng Q, Li B, Li T, Feng X (2017) A multiscale crack-bridging model of cellulose nanopaper. J Mech Phys Solids 103:22–39. https://doi.org/10.1016/j.jmps.2017.03.004

Meng Q, Wang TJ (2019) Mechanics of strong and tough cellulose nanopaper. Appl Mech Rev 71:040801. https://doi.org/10.1115/1.4044018

Moon RJ, Martini A, Nairn J et al (2011a) Cellulose nanomaterials review: Structure, properties and nanocomposites

Moon RJ, Martini A, Nairn J, Youngblood J (2011) Cellulose nanomaterials review: structure, properties and nanocomposites. Chem Soc Rev 40:3941–3994. https://doi.org/10.1039/c0cs00108b

Motamedian HR, Halilovic AE, Kulachenko A (2019) Mechanisms of strength and stiffness improvement of paper after PFI refining with a focus on the effect of fines. Cellulose 26:4099–4124. https://doi.org/10.1007/s10570-019-02349-5

Müller FA, Müller L, Hofmann I et al (2006) Cellulose-based scaffold materials for cartilage tissue engineering. Biomaterials 27:3955–3963. https://doi.org/10.1016/j.biomaterials.2006.02.031

Ogawa Y (2019) Electron microdiffraction reveals the nanoscale twist geometry of cellulose nanocrystals. Nanoscale 11:21767–21774. https://doi.org/10.1039/c9nr06044h

Plimpton S (1995) Fast parallel algorithms for short-range molecular dynamics. J Comput Phys 117:1–19

Qin X, Feng S, Meng Z, Keten S (2017) Optimizing the mechanical properties of cellulose nanopaper through surface energy and critical length scale considerations. Cellulose 24:3289–3299. https://doi.org/10.1007/s10570-017-1367-x

Ray U, Zhu S, Pang Z, Li T (2020) Mechanics design in cellulose-enabled high-performance functional materials. Adv Mater 2002504:1–22. https://doi.org/10.1002/adma.202002504

Redinz JA, Guimarães PRC (1997) The fractal nature of wood revealed by water absorption. Wood Fiber Sci 29:333–339

Rouhi S (2019) On the mechanical properties of the graphdiyne nanotubes: a molecular dynamics investigation. Braz J Phys 49:654–666. https://doi.org/10.1007/s13538-019-00673-6

Saito T, Kuramae R, Wohlert J et al (2013) An ultrastrong nanofibrillar biomaterial: the strength of single cellulose nanofibrils revealed via sonication-induced fragmentation. Biomacromolecules 14:248–253. https://doi.org/10.1021/bm301674e

Sehaqui H, Zhou Q, Ikkala O, Berglund LA (2011) Strong and tough cellulose nanopaper with high specific surface area and porosity. Biomacromolecules 12:3638–3644. https://doi.org/10.1021/bm2008907

Shin S, Hyun J (2017) Matrix-assisted three-dimensional printing of cellulose nanofibers for paper microfluidics. ACS Appl Mater Interfaces 9:26438–26446. https://doi.org/10.1021/acsami.7b07609

Shishehbor M, Zavattieri PD (2019) Effects of interface properties on the mechanical properties of bio-inspired cellulose nanocrystal (CNC)-based materials. J Mech Phys Solids 124:871–896. https://doi.org/10.1016/j.jmps.2018.12.002

Sinko R, Keten S (2015) Traction – separation laws and stick—slip shear phenomenon of interfaces between cellulose

nanocrystals. J Mech Phys Solids 78:526–539. https://doi.org/10.1016/j.jmps.2015.02.012
Sinko R, Mishra S, Ruiz L et al (2014) Dimensions of biological cellulose nanocrystals maximize fracture strength. ACS Macro Lett 3:64–69. https://doi.org/10.1021/mz400471y
Song J, Chen C, Yang Z et al (2018) Highly compressible, anisotropic aerogel with aligned cellulose nanofibers. ACS Nano 12:140–147. https://doi.org/10.1021/acsnano.7b04246
Song J, Chen C, Zhu S et al (2018) Processing bulk natural wood into a high-performance structural material. Nature 554:224–228. https://doi.org/10.1038/nature25476
Srinivas G, Cheng X, Smith JC (2011) A solvent-free coarse grain model for crystalline and amorphous cellulose fibrils. J Chem Theory Comput 7:2539–2548. https://doi.org/10.1021/ct200181t
Svensson A, Nicklasson E, Harrah T et al (2005) Bacterial cellulose as a potential scaffold for tissue engineering of cartilage. Biomaterials 26:419–431. https://doi.org/10.1016/j.biomaterials.2004.02.049
Sydney Gladman A, Matsumoto EA, Nuzzo RG et al (2016) Biomimetic 4D printing. Nat Mater 15:413–418. https://doi.org/10.1038/nmat4544
Szymanska-Chargot M, Chylinska M, Gdula K et al (2017) Isolation and characterization of cellulose from different fruit and vegetable pomaces. Polymers (Basel). https://doi.org/10.3390/polym9100495
Usov I, Nyström G, Adamcik J et al (2015) Understanding nanocellulose chirality and structure-properties relationship at the single fibril level. Nat Commun. https://doi.org/10.1038/ncomms8564
Wang S, Jiang F, Xu X et al (2017) Super-strong, super-stiff macrofibers with aligned, long bacterial cellulose nanofibers. Adv Mater 29:1702498(1–8). https://doi.org/10.1002/adma.201702498
Wang S, Li T, Chen C et al (2018) Transparent, anisotropic biofilm with aligned bacterial cellulose nanofibers. Adv Funct Mater 28:1707491(1–10). https://doi.org/https://doi.org/10.1002/adfm.201707491
Wang X, Pang Z, Chen C et al (2020) All-natural, degradable, rolled-up straws based on cellulose micro- and nano-hybrid fibers. Adv Funct Mater 30:1–9. https://doi.org/10.1002/adfm.201910417
Wu X, Moon RJ, Martini A (2013) Crystalline cellulose elastic modulus predicted by atomistic models of uniform deformation and nanoscale indentation. Cellulose 20:43–55. https://doi.org/10.1007/s10570-012-9823-0
Wu X, Moon RJ, Martini A (2014) Tensile strength of Iβ crystalline cellulose predicted by molecular dynamics simulation. Cellulose 21:2233–2245. https://doi.org/10.1007/s10570-014-0325-0
Xia W, Qin X, Zhang Y et al (2018) Achieving enhanced interfacial adhesion and dispersion in cellulose nanocomposites via amorphous interfaces. Macromolecules 51:10304–10311. https://doi.org/10.1021/acs.macromol.8b02243
Yousefi H, Faezipour M, Hedjazi S et al (2013) Comparative study of paper and nanopaper properties prepared from bacterial cellulose nanofibers and fibers/ground cellulose nanofibers of canola straw. Ind Crops Prod 43:732–737. https://doi.org/10.1016/j.indcrop.2012.08.030
Zhang Q, Chen C, Chen W et al (2019) Nanocellulose-enabled, all-nanofiber, high-performance supercapacitor. ACS Appl Mater Interfaces 11:5919–5927. https://doi.org/10.1021/acsami.8b17414
Zhang Y, Luo W, Wang C et al (2017) High-capacity, low-tortuosity, and channel-guided lithium metal anode. Proc Natl Acad Sci USA 114:3584–3589. https://doi.org/10.1073/pnas.1618871114
Zhou Y, Chen C, Zhu S et al (2019) A printed, recyclable, ultra-strong and ultra-tough graphite structural material. Mater Today 30:17–25
Zhu H, Fang Z, Preston C et al (2014) Transparent paper: fabrications, properties, and device applications. Energy Environ Sci 7:269–287. https://doi.org/10.1039/c3ee43024c
Zhu H, Zhu S, Jia Z et al (2015) Anomalous scaling law of strength and toughness of cellulose nanopaper. PNAS 112:8971–8976. https://doi.org/10.1073/pnas.1502870112
Zhu M, Song J, Li T et al (2016) Highly anisotropic, highly transparent wood composites. Adv Mater 28:5181–5187. https://doi.org/10.1002/adma.201600427
Zhu M, Wang Y, Zhu S et al (2017) Anisotropic, transparent films with aligned cellulose nanofibers. Adv Mater 29:1606284(1–8). https://doi.org/https://doi.org/10.1002/adma.201606284
Zhu S, Huang Y, Li T (2014) Extremely compliant and highly stretchable patterned graphene. Appl Phys Lett. https://doi.org/10.1063/1.4874337